Surface hardening of TiZrNbHfTa high entropy alloy via oxidation

Daniel Dickes, Beyza Öztürk, Felix Baier, Easo P George, Rainer Völkl, Mathias C Galetz, Uwe Glatzel, Pascal Berger

To cite this version:

Daniel Dickes, Beyza Öztürk, Felix Baier, Easo P George, Rainer Völkl, et al.. Surface hardening of TiZrNbHfTa high entropy alloy via oxidation. Corrosion Science, 2023, 217, pp.111159. 10.1016/j.corsci.2023.111159 . hal-04287944

HAL Id: hal-04287944
https://hal.science/hal-04287944

Submitted on 15 Nov 2023

Surface hardening of TiZrNbHfTa high entropy alloy via oxidation

*Daniel Dickes[a), Beyza Öztürk[b), Felix Baier[c), Pascal Berger[d), Easo P. George[e),f), Rainer Völkl[a), Mathias C. Galetz[b), Uwe Glatzel[a)**

a) University of Bayreuth, Metals and Alloys, Prof.-Rüdiger-Bormann-Straße 1, 95447 Bayreuth, Germany
E-mail: uwe.glatzel@uni-bayreuth.de

b) DECHEMA-Forschungsinstitut, Materials and Corrosion, Theodor-Heuss-Allee 25, 60486 Frankfurt am Main, Germany

c) University of Bayreuth, Experimental Physics XI, Universitätsstraße 30, 95448 Bayreuth, Germany

d) Université Paris-Saclay, CEA, CNRS, NIMBE, 91191 Gif-sur Yvette, France

e) Oak Ridge National Laboratory, Materials Science and Technology Division, Oak Ridge, TN 37831, USA

f) University of Tennessee, Materials Science and Engineering Department, Knoxville, TN 37996, USA

Abstract

We investigate the oxidation of TiZrNbHfTa high entropy alloy between 550 °C and 650 °C as a surface hardening method. Coarse-grained specimens with grain boundaries perpendicular to the surface exhibit catastrophic oxidation, while ultrafine-grained, cold-rolled specimens show a continuous mass gain and the formation of an adherent, µm-sized, vitreous oxide layer. Underneath, TiZrNbHfTa decomposes into a bcc- and an hcp-phase, while selective internal oxidation of hafnium and zirconium occurs upon oxygen inward diffusion. Oxygen concentration- and microhardness-depth profiles confirm an increase in oxygen concentration and hardness at the surface, raising the initial hardness by four times to 1522±64 HV 0.5.

Keywords

A. alloy
C. high temperature corrosion
C. oxidation
C. internal oxidation
C. kinetic parameters
C. hardening

1. Introduction

The high entropy alloy TiZrNbHfTa was first reported by Senkov et al. [1] in 2011 and consists of five refractory elements in equimolar composition. It can have a single-phase bcc structure at ambient conditions [1,2] and is one of few refractory high entropy alloys showing ductile tensile behavior at room temperature [3,4]. Due to this ductility, its low Young's modulus, high compressive yield strength, and good fatigue behavior, TiZrNbHfTa is discussed as an implant material [5]. In addition to good biocompatibility, a high wear resistance is required for biomaterials used in artificial joints to avoid revision surgeries, e.g., due to inflammations caused by wear debris [6]. Sputtered TiZrNbHfTa nitride and carbide coatings proved to enhance the wear behavior of Ti6Al4V [7]. Also, sputtered $Ti_{1.5}ZrNb_{0.5}Hf_{0.5}Ta_{0.5}$ amorphous films on Ti6Al4V could improve the surface mechanical properties [8]. Oxidation has been successfully used to improve the wear properties of Ti6Al4V [9] and Zr alloys [10–13], raising the question if this method is also suitable for TiZrNbHfTa.

Owing to the vast composition space of refractory high entropy alloys, the number of studied refractory high entropy alloys has tremendously increased over the past years [14], including studies focusing on oxidation. Recent reviews provide an overview of these oxidation studies [14–18]. It turns out that the oxidation behavior of high entropy alloys is strongly composition dependent and can be altered by adding or replacing elements. This has been proven by a systematic study of the elemental effects of Al, Cr, Mo, Nb, Ta, Ti, and Zr [19], with Al and Cr being capable of forming protective Al_2O_3 and Cr_2O_3 oxide layers [20]. Regarding elements present in TiZrNbHfTa, Lo et al. [19] identified Ti as beneficial for the oxidation resistance, while Zr degraded the oxidation resistance. According to their work [19], Ta is slightly beneficial compared to Nb because it reduces the oxygen intake of the bulk alloy. For equimolar TiZrNbHfTa and similar alloys containing the five elements Ti, Zr, Nb, Hf, and Ta, previous oxidation studies have reported severe spallation and mass loss during oxidation at elevated temperatures in air [5,20–22]. This is a common phenomenon in refractory high entropy alloys [15].

This work aims to understand under which conditions a hard, adherent oxide layer could form on TiZrNbHfTa through oxidation. For this purpose, the oxidation behavior of TiZrNbHfTa specimens with different microstructures is studied in the temperature range of 550 °C to 650 °C, including an assessment of the reaction kinetics and the obtained surface hardness.

2. Materials and methods

Material synthesis

Three different processing routes are deployed to obtain TiZrNbHfTa alloy specimens with different microstructures. The first specimen type is TiZrNbHfTa, just after arc melting, herein called the as-cast state. A Bühler vacuum arc-melting system is used to alloy the pure constituent elements on a cooled copper plate to an ingot. Each ingot is flipped and re-melted five times to ensure homogeneity. An AgieCharmilles Cut 200 SP wire-cut electrical discharge machine is used to slice the ingots into ~1 mm thick sheets. The second specimen type, called rolled state, is TiZrNbHfTa derived through cold-rolling an arc-melted ingot after 48 h of homogenization at 1200 °C under vacuum, as described by Gadelmeier et al. [23]. A final sheet thickness of ~1 mm is obtained after a ~90 % thickness reduction during the rolling process. The third specimen type, called rolled & annealed state, results from annealing the rolled state for at 1200 °C in vacuum, followed by rapid cooling in water. Electrical discharge machining is used to cut the as-cast, rolled, and rolled & annealed sheets into specimens. All specimens are ground down to P1200 SiC paper and cleaned in ethanol before oxidation experiments. This ensures comparable surface conditions and avoids an impact of the processing route, e.g., through a potential skin hardening effect during cold-rolling.

Oxidation

Oxidation is either performed in a laboratory furnace or in a thermogravimetric analysis (TGA) setup. During TGA, the oxidation is executed in synthetic air atmosphere (50 ml/min) following a heat up from room temperature to the desired temperature at a heating rate of 20 K/min. A NETZSCH STA 449F3 using inert gas during the heat-up phase is used for the comparative thermogravimetric analysis of as-cast, rolled, and rolled & annealed specimens at 600 °C for 24 h. A NETZSCH STA 449F5 using artificial air during heat-up is deployed to oxidize rolled specimens at 550 °C, 600 °C, and 650 °C for 24 h to derive the kinetics of mass change. Specimens not requiring a weight measurement during oxidation, e.g., for the thickness determination of an oxygen-enriched zone near the surface, are oxidized in a pre-heated furnace in laboratory air and removed for cooling outside the oven. Specimens that are oxidized at 550 °C, 575 °C, 600 °C, 625 °C, and 650 °C with oxidation durations of 1 h, 2 h, 4 h, and 8 h, respectively, are used to determine the growth kinetics of such an oxygen-enriched zone.

Analysis

The chemical composition of as-cast, rolled, and rolled & annealed TiZrNbHfTa is determined using an Orbis PC µX-ray fluorescence analysis device combined with a Horiba EMGA 620 W/C carrier hot gas extraction analyzer to account for oxygen and nitrogen.

An X-ray diffraction analysis (XRD) of the initial as-cast, rolled, and rolled & annealed TiZrNbHfTa is performed using a Bruker D8 Discovery with a Cu $K_{\alpha I}$ radiation source, a diffraction angle range of 20 ° to 140 °, and a step size of 0.01 °. In addition, the oxide layer and the non-oxygen-enriched substrate of as-cast, rolled, and rolled & annealed specimens after oxidation (600 °C, 24 h) are analyzed. Before and after oxidation, cross-section micrographs of each specimen type are investigated using backscattered electron imaging on a Zeiss 1540 ESB Cross Beam scanning electron microscope (SEM) and a Jeol JXA-8100 electron probe micro analyzer (EPMA). The surface normalized mass change during oxidation of as-cast, rolled, and rolled & annealed TiZrNbHfTa is compared using TGA, as detailed in the previous section. The growth kinetics of an oxygen-enriched zone is derived from cross-section micrographs after 1 h, 2 h, 4 h, and 8 h of oxidation in the temperature range of 550 °C to 650 °C. Four to eight SEM images per cross-section, leading to a monitored surface of approx. 450 µm width with more than 400 measurement points, were considered to average the thickness of the oxygen-enriched zone. Qualitative X-ray photoelectron spectroscopy (XPS) is performed on the surface of one oxidized rolled TiZrNbHfTa specimen (600 °C, 1 h) with a Physical Electronics PHI 5000 VersaProbe III. XPS measurements are also performed on a cross-section micrograph (600 °C, 24 h) in the oxygen-enriched zone demarcated from the surrounding using an applied Platinum mask and 200 min of sputtering with argon ions at 3 kV. Nuclear reaction analysis (NRA) is used to exemplarily investigate the quantitative oxygen concentration-depth profile of a rolled TiZrNbHfTa specimen oxidized at 600 °C for 8 h. A deuteron beam at 920 keV with a beam size of 4.5 µm x 3.5 µm is used to generate an oxygen intensity mapping of 200 µm x 150 µm with a pixel size of 2 µm x 2 µm. A quantitative depth profile is derived from this mapping using a SiO_2 reference standard. The corresponding microhardness-depth profile is obtained from Martens hardness measurements on the cross-section micrograph. A Fischerscope H100 with a Vickers indenter was deployed in depth-controlled mode with an indentation depth of 0.2 µm. In addition, the surface hardness of this specimen is assessed from 18 HV0.5 Vickers hardness measurements (mean value ± 95% confidence level).

3. Results and discussion

Characterization of initial material

Table 1 shows that the alloy composition deviates less than ± 2 at.% from the equimolar state in all three states. The oxygen concentration of the as-cast state is slightly lower than in the rolled and the rolled & annealed state. No significant difference in nitrogen concentration is evident.

[TABLE 1]

As far as assessable with XRD measurements [24], all specimens in their initial state are single-phase bcc (not shown here). The XRD patterns are in good agreement with database values for TiZrNbHfTa (ICDD 04-018-5441) [1].

Figure 1 shows the microstructure of the specimens before oxidation. Despite similar alloy composition and crystal structure, significant differences are apparent. In the as-cast state (Figure 1 a)) and the rolled & annealed state (Figure 1 c)), distinctive, coarse grains are visible in the micrographs, with sub-grain boundaries present in the as-cast state. The grain size in the as-cast state is 90±33 µm, while it is 47±22 µm for the rolled & annealed state. Due to the heavy deformation during the rolling process, the rolled state is ultrafine-grained (200±120 nm) with thin grains preferentially oriented parallel to the surface (Figure 1 b)), similar to the observations of Senkov et al. [4].

[FIGURE 1]

Oxidation behavior

Figure 2 provides the result of the thermogravimetric analysis. In the case of the coarse-grained as-cast and rolled & annealed state, a mass gain is only visible until an oxidation duration of approx. 3.5 h. After that, spallation occurs, leading to mass loss. Such catastrophic oxidation of TiZrNbHfTa has been reported in the literature before [5,20,21]. However, the mass gain is continuous for the ultrafine-grained rolled state and spallation is not observed in this case. This implies that the microstructure has a strong influence on the oxidation behavior.

[FIGURE 2]

Several phenomena must be considered to derive the reason for the different oxidation behavior observed for coarse-grained and ultrafine-grained TiZrNbHfTa. According to Schütze [25], the failure of an oxide layer during oxidation can be associated with different types of stresses: intrinsic growth stresses, geometrically induced growth stresses, thermal stresses, and external stresses. Given the identical elemental composition of the coarse-grained as-cast and rolled & annealed state, as well as the ultrafine-grained rolled state, the oxide types expected to form during oxidation are also identical in all three cases. Therefore, from a macroscopic perspective, the occurring intrinsic growth stresses, geometrically induced growth stresses, thermal stresses, and external stresses should be comparable. However, differences regarding intrinsic growth stresses during the oxidation process can occur from a microscopic viewpoint, including intrinsic growth stresses due to oxygen diffusion into and dissolution in the metal [26] or due to phase and compositional changes [27]. Both aspects are addressed in the following.

Figure 1 d)-f) shows backscattered SEM images of the specimens after oxidation. All specimens exhibit a darker appearing region at the surface, indicating the presence of a light element such as oxygen. The qualitative EPMA oxygen mappings, shown in Figure 1 g)-i), confirm the existence of oxygen-enriched zones near the surface. The oxygen-enriched zone is largest in the case of the ultrafine-grained rolled state due to the absence of spallation during oxidation. Figure 3 a) provides a magnified excerpt of the oxygen-enriched zone obtained for ultrafine-grained, rolled TiZrNbHfTa. The backscattered SEM images reveal a compact surface oxide layer of approx. 1 µm thickness. Underneath this compact layer, the oxygen-enriched zone is characterized by a two-phase microstructure on a nanometer scale with one phase appearing darker, i.e., oxygen-rich. From a macroscopic perspective, the oxygen-enriched zone appears to be homogeneous. This agrees with the corresponding EPMA oxygen mapping (Figure 1 h)), indicating that the oxygen ingress occurs homogenously over the whole specimen during oxidation of ultrafine-grained, rolled TiZrNbHfTa. In contrast, pronounced grain boundaries perpendicular to the surface are present in the case of coarse-grained TiZrNbHfTa, where they act as preferred oxygen diffusion pathways, as visible in Figure 3 b). It can be concluded that ultrafine-grained and coarse-grained TiZrNbHfTa exhibit significantly different oxygen inward diffusion during oxidation.

[FIGURE 3]

The qualitative EPMA oxygen mappings, shown in Figure 1 g)-i) reveal no increased oxygen presence in the substrate underneath the oxygen-enriched zone. Nevertheless, the substrate exhibits visible changes at the grain boundaries in the rolled & annealed state (Figure 1 f)) and at the grain and sub-grain boundaries in the as-cast state (Figure 1 d)). A closer investigation of the substrate, as shown in Figure 4, reveals that at least one new phase forms at the grain and sub-grain boundaries in the substrate of the as-cast specimen during oxidation, which has also been observed by Stepanov et al. [28]. The substrate of the rolled specimen is also no longer single-phase but homogenously decomposed into a two-phase microstructure. In the case of the rolled & annealed state, a lamellar microstructure consisting of two phases forms at the grain boundaries and grows into the grains. Occasionally, the formation of a new phase occurs also inside the grains, comparable to observations by Chen et al. [29].

[FIGURE 4]

Figure 5 a) shows a TiZrNbHfTa phase diagram derived from Calphad calculations using ThermoCalc with the TC-Ni8 database. Above about 1020 °C, the alloy is expected to be single-phase body-centered cubic, i.e., bcc1. While precipitation of a second body-centered cubic bcc2 phase starts below 1020 °C, at temperatures lower than approx. 700 °C, the initial bcc1 phase is expected to completely decompose into the bcc2 phase and a hexagonal closed-packed hcp1 phase. The decomposition of the bcc1 phase into a NbTa-rich bcc2 phase and a HfZr-rich hcp1 phase at temperatures below 1020 °C has recently been predicted by first principle calculations

[30] and is experimentally confirmed [29,31]. Figure 5 b) depicts XRD measurements of the non-oxygen-enriched substrates after oxidation (600 °C, 24 h). Peaks of a bcc1 phase (a = 340.7 pm), a bcc2 phase (a = 333.8 pm), and a hcp1 phase (c = 505.9 pm, a = 318.7 pm) are identified in the case of the as-cast and the rolled & annealed state. The ultrafine-grained rolled state only comprises the bcc2 and the hcp1 phase, indicating that the decomposition process is fully completed. This is due to the ultrafine-grained microstructure providing a high number of grain boundaries, which act as nucleation sites and diffusion pathways, accelerating the decomposition process [31]. Based on the microstructure (Figure 4) and XRD analysis (Figure 5 b)), it can be concluded that ultrafine-grained TiZrNbHfTa rapidly decomposes, leading to a homogeneous, two-phase microstructure on the nanometer scale throughout the specimen, while a phase decomposition occurs only localized at the grain boundaries in coarse-grained TiZrNbHfTa.

[FIGURE 5]

The catastrophic oxidation behavior of coarse-grained, as-cast and rolled & annealed TiZrNbHfTa is linked to the presence of pronounced grain boundaries.

Excluding microstructure effects, Gorr et al. [15] assign the oxidation of TiZrNbHfTa to a mechanism consisting of: oxygen dissolution in the metal and crack formation, internal oxidation and cracking of an outer layer of the metal, and oxidation of the broken-up layer. They attribute the local crack formation to stresses caused by an anisotropic lattice distortion due to interstitials occupying octahedral sites in the bcc crystal, as described by Kofstad [32]. Sheikh et al. [20] assign the catastrophic oxidation behavior of $Ti_{1.5}ZrNb_{0.5}Hf_{0.5}Ta_{0.5}$ to the lack of formation of a protective oxide scale due to a mismatch in volume expansion between the formed oxides and the substrate. In addition, they mention intergranular oxidation through inward diffusing oxygen, assisted by grain and subgrain boundaries, as a cause for the catastrophic oxidation behavior [20]. This work underlines that the catastrophic oxidation of coarse-grained, as-cast and rolled & annealed TiZrNbHfTa is linked to pronounced grain boundaries acting as sites for localized phase decomposition, localized oxygen inward diffusion, and localized oxygen dissolution or internal oxidation. As summarized in Figure 6, these effects lead to localized internal stresses at the grain boundaries resulting in intergranular cracking and catastrophic oxidation.

[FIGURE 6]

Such localized internal stresses and their negative consequences are not expected for ultrafine-grained, rolled TiZrNbHfTa because the phase decomposition occurs rapidly throughout the specimen on a nanometer scale. This results in a quasi-homogeneous oxygen inward diffusion over the entire surface, leading to an adherent surface oxide layer on top of an oxygen-enriched zone.

The XPS surface analysis shown in Figure 7 a) reveals that the compact surface layer consists of simple monometallic oxides, namely TiO_2, ZrO_2, Nb_2O_5, HfO_2, and Ta_2O_5, while none of the elements contained in TiZrNbHfTa are present in metallic state directly at the surface. These oxides have also been observed in XPS studies on TiZrNbHfTa oxidized in air at ambient temperature [8,33] and at 800 °C [5].

[FIGURE 7]

However, the XRD analysis shown in Figure 8 does not indicate the presence of these oxides. Figure 8 b) shows that the theoretical reflex positions of the most likely monometallic oxides ZrO_2 (ICDD 04-015-6852) [34], HfO_2 (ICDD 00-034-0104) [35], and TiO_2 (ICDD 00-021-1276) [36] do not unambiguously match the diffractogram. Other crystal structures reported in the literature, such as the $HfTiO_4$ or $ZrTiO_4$ structure [20], are neither present since complex oxides typically form only after prolonged oxidation [15]. Regardless of the initial microstructure of TiZrNbHfTa, only few, broad peaks with a poor peak-to-background ratio are apparent. This implies the absence of a long-range crystalline order, i.e., a vitreous-type oxide layer. The formation of such locally ordered oxide crystallites in a disordered oxide matrix has been previously confirmed for a different high entropy alloy at 400 °C [37] and can explain our observation.

Underneath the compact oxide layer, the cross-sectional XPS analysis shown in Figure 7 b) indicates selective internal oxidation of Zr and Hf, both preferentially occurring in the hcp1 phase and thus explaining the darker appearing phase in the backscattered SEM images (Figure 3 a)).

[FIGURE 8]

According to the experimental resuluts, oxidation of ultrafine-grained, rolled TiZrNbHfTa at 600 °C comprises the formation of a µm-sized, compact, vitreous oxide layer and a rapid phase decomposition underneath, leading to selective internal oxidation of Hf and Zr upon oxygen inward diffusion, as schematically visualized in Figure 9. The ultrafine-grained microstructure, induced to TiZrNbHfTa during cold-rolling, is favorable in terms of the oxidation behavior and can avoid catastrophic oxidation. This is due to the absence of a localized phase decomposition, localized oxygen ingress, and localized oxygen dissolution or internal oxidation at pronounced grain boundaries. A positive effect of a deformation-induced microstructure refinement on the oxidation behavior has also been reported for AlCoCrFeNi high entropy alloy [38].

[FIGURE 9]

The absence of spallation during oxidation of ultrafine-grained TiZrNbHfTa allows determining the time t and temperature T dependent kinetics of the area-specific mass gain $\frac{\Delta m}{A}$. Parabolic behavior can be assumed to determine the rate constants k_m from the different TGA curves shown in Figure 10 a) following:

$$\left(\frac{\Delta m}{A}\right)^2 = k_m \cdot t \qquad (1)$$

Figure 10 b) shows the temperature dependency of k_m based on an Arrhenius type equation (2) yielding an activation energy Q_m of 178 kJmol^{-1} and a factor k_{m0} of 796.6 kg^{2}m^{-4}s^{-1} for ultrafine-grained, rolled TiZrNbHfTa in the investigated temperature range.

$$k_m = k_{m0} \cdot e^{\frac{-Q_m}{RT}} \tag{2}$$

As visible in Figure 10 c), the thickness s of the oxygen-enriched zone, including the compact oxide layer and the region of selective internal oxidation, also grows parabolically:

$$s^2 = k_s \cdot t \tag{3}$$

The Arrhenius plot in Figure 10 d) shows the temperature dependency of the rate constant k_s based on an Arrhenius type equation (4) yielding an activation energy Q_s of 139 kJmol^{-1} and a factor k_{s0} of 6.7 × 10^{-6} m.

$$k_s = k_{s0} \cdot e^{\frac{-Q_s}{RT}} \tag{4}$$

The parabolic increase of the area-specific mass gain and the thickness of the oxygen-enriched zone indicate that the oxidation process is diffusion-controlled [32], in this case by inward diffusion of oxygen. An attempt is made to convert the rate constants k_m into rate constants k_s using equation (1) and (2) and assuming volume constancy of the specimen over time t and temperature T:

$$\frac{\frac{\Delta m(t,T)}{A}}{s(t,T)} = \frac{\sqrt{k_m(T)\cdot t}}{\sqrt{k_s(T)\cdot t}} \Rightarrow \Delta\rho(T) = \sqrt{\frac{k_m(T)}{k_s(T)}} \tag{5}$$

With equation (5), the experimentally determined mass change, and the thickness data of the oxygen-enriched zones, a mean $\Delta\rho(T)$ is calculated for each temperature, as shown in Figure 10 e). This mean $\Delta\rho(T)$ is then used to convert the respective k_m into rate constants k_s according to equation (5). The Arrhenius plot in Figure 10 f) yields the combined activation energy Q_{sc} of 143 kJmol^{-1} and a factor k_{sc0} of 1.2 × 10^{-5} m.

While any amount of inward diffusing oxygen is accounted for in the thermogravimetric measurements, oxygen ingress into the specimen does not immediately lead to a visible increase in the thickness of the oxygen-enriched zone in the backscattered SEM images. This explains the higher activation energy observed for Q_m in contrast to Q_s and Q_{sc}.

[FIGURE 10]

Surface properties

Due to their catastrophic oxidation behavior leading to an absence of a hard, adherent oxide layer after oxidation, coarse-grained, as-cast and rolled & annealed material is not further considered. Instead, oxidation at 600 °C of rolled, ultrafine-grained TiZrNbHfTa proves to be a suitable method to enhance the surface mechanical properties, which are studied in more detail in the following. A microhardness-depth profile of a specimen oxidized for 8 h is given in Figure 11. The highest microhardness of 10.9 GPa is achieved in the compact oxide layer at the surface, followed by a decrease in the region of selective internal oxidation until 30 µm depth, and a gradual microhardness decrease towards the substrate hardness (3.9 GPa). Due to the phase decomposition during the oxidation process also occurring in the non-oxygen-enriched substrate region, the substrate hardness is increased compared to the initial rolled state (3.3 GPa), as also observed by Stepanov et al. [28]. The microhardness-depth profile obtained during oxidation correlates with the oxygen concentration-depth profile expressed in terms of oxygen stoichiometry x in $Ti_1Zr_1Nb_1Hf_1Ta_1O_x$, as shown in Figure 11. If all elements are oxidized to their most stable oxides, an oxygen stoichiometry x of 11 would be expected for the compact surface oxide layer due to the formation of TiO_2, ZrO_2, Nb_2O_5, HfO_2, and Ta_2O_5 in equimolar TiZrNbHfTa. According to the XPS results, the measured value at the surface is 7.5. One reason for this deviation is that the µm-sized compact oxide layer cannot be sufficiently resolved with the given NRA mapping resolution. Secondly, the presence of elements in metallic state in depths not covered by surface XPS analysis is possible. In the region of selective internal oxidation, the oxygen stoichiometry levels out at 4, which, under the assumption of equimolar composition, is equivalent to an oxygen concentration of approx. 44 at.%. Hence, the oxygen concentration is above the solubility limit of oxygen in Ti (33 at.% [39]), Zr (29 at.% [40]), or Hf (20 at.% [41]), which indicates the formation of oxides. This is in good agreement with the XPS analysis confirming the formation of ZrO_2 and HfO_2, the most stable oxides in the material system.

[FIGURE 11]

The surface hardness of an ultrafine-grained, rolled specimen after 8 h of oxidation at 600 °C is 1522±64 HV 0.5. This is more than four times harder than the initial specimen hardness of 347±5 HV 0.5, approx. three times harder than a hardness increase solely due to the formation of hcp precipitates during aging at 600 °C reported by Stepanov et al. [28], and more than two times harder than laser-treated TiZrNbHfTa with refined grains and multiple phases at the surface [42].

5. Conclusion

In this study, the oxidation behavior of TiZrNbHfTa high entropy alloy specimens having different microstructures was studied in the temperature range of 550 °C to 650 °C, revealing that:

- Coarse-grained, as-cast and rolled & annealed TiZrNbHfTa exhibit catastrophic oxidation behavior due to the presence of pronounced grain boundaries perpendicular to the surface, which act as preferred sites for localized oxygen inward diffusion and phase decomposition resulting in localized stress concentrations and intergranular cracking.
- A compact, adherent, µm-sized, vitreous oxide layer containing TiO_2, ZrO_2, Nb_2O_5, HfO_2, and Ta_2O_5 forms at the surface of rolled, ultrafine-grained TiZrNbHfTa accompanied by a rapid phase decomposition of the underneath substrate and selective internal oxidation of Hf and Zr.
- Oxidation of rolled TiZrNbHfTa at 600 °C for 8 h increases the surface hardness from 347±5 HV 0.5 to 1522±64 HV 0.5, with the hardened zone being correlated to the oxygen concentration-depth profile.

7. Acknowledgments

We are grateful for the financial support of the German Research Foundation DFG (project number 270293189; GL 181/41-2 and GA 1704/12-2). The access to the XPS/UPS facility (PHI 5000 VersaProbe III system) at the Device Engineering KeyLab at the Bavarian Polymer Institute, University of Bayreuth, is gratefully acknowledged. E.P.G. was supported by the U.S. Department of Energy, Office of Science, Basic Energy Sciences, Materials Sciences and Engineering Division. We thank C. Gadelmeier, University of Bayreuth, for producing the as-cast TiZrNbHfTa ingot.

8. Declaration of conflict

The authors declare no potential conflicts of interest with respect to the research, authorship, and/or publication of this article.

9. Data availability

Selected raw data required to reproduce these findings are available to download from http://dx.doi.org/10.17632/4wc88th7j8.1. The processed data cannot be shared at this time as the data also forms part of an ongoing study.

Literature

[1] O.N. Senkov, J.M. Scott, S.V. Senkova, D.B. Miracle, C.F. Woodward, Microstructure and room temperature properties of a high-entropy TaNbHfZrTi alloy, Journal of Alloys and Compounds 509 (2011) 6043–6048. https://doi.org/10.1016/j.jallcom.2011.02.171.

[2] J.P. Couzinié, G. Dirras, L. Perrière, T. Chauveau, E. Leroy, Y. Champion, I. Guillot, Microstructure of a near-equimolar refractory high-entropy alloy, Materials Letters 126 (2014) 285–287. https://doi.org/10.1016/j.matlet.2014.04.062.

[3] G. Dirras, L. Lilensten, P. Djemia, M. Laurent-Brocq, D. Tingaud, J.-P. Couzinié, L. Perrière, T. Chauveau, I. Guillot, Elastic and plastic properties of as-cast equimolar TiHfZrTaNb high-entropy alloy, Materials Science and Engineering: A 654 (2016) 30–38. https://doi.org/10.1016/j.msea.2015.12.017.

[4] O.N. Senkov, S.L. Semiatin, Microstructure and properties of a refractory high-entropy alloy after cold working, Journal of Alloys and Compounds 649 (2015) 1110–1123. https://doi.org/10.1016/j.jallcom.2015.07.209.

[5] M. Gueye, S. Ammar-Merah, S. Nowak, P. Decorse, A. Chevillot-Biraud, L. Perrière, J.P. Couzinie, I. Guillot, G. Dirras, Study of the stability under in vitro physiological conditions of surface silanized equimolar HfNbTaTiZr high-entropy alloy: A first step toward bio-implant applications, Surface and Coatings Technology 385 (2020) 125374. https://doi.org/10.1016/j.surfcoat.2020.125374.

[6] M. Geetha, A.K. Singh, R. Asokamani, A.K. Gogia, Ti based biomaterials, the ultimate choice for orthopaedic implants – A review, Progress in Materials Science 54 (2009) 397–425. https://doi.org/10.1016/j.pmatsci.2008.06.004.

[7] V. Braic, M. Balaceanu, M. Braic, A. Vladescu, S. Panseri, A. Russo, Characterization of multi-principal-element (TiZrNbHfTa)N and (TiZrNbHfTa)C coatings for biomedical applications, J. Mech. Behav. Biomed. Mater. 10 (2012) 197–205. https://doi.org/10.1016/j.jmbbm.2012.02.020.

[8] N.S. Peighambardoust, A.A. Alamdari, U. Unal, A. Motallebzadeh, In vitro biocompatibility evaluation of Ti1.5ZrTa0.5Nb0.5Hf0.5 refractory high-entropy alloy film for orthopedic implants: Microstructural, mechanical properties and corrosion behavior, Journal of Alloys and Compounds 883 (2021) 160786. https://doi.org/10.1016/j.jallcom.2021.160786.

[9] D. Dickes, B. Öztürk, R. Völkl, M.C. Galetz, U. Glatzel, Improving the adhesion of a hard oxide layer on Ti6Al4V by a three-step thermal oxidation process, Adv. Eng. Mater. (2021) 2100864. https://doi.org/10.1002/adem.202100864.

[10] M. Mosbacher, M. Holzinger, M. Galetz, U. Glatzel, The Influence of Oxide Color on the Surface Characteristics of Zirconium Alloy ZrNb7 (wt%) After Different Heat Treatments, Oxidation of Metals 95 (2021) 377–388. https://doi.org/10.1007/s11085-021-10030-1.

[11] M. Mosbacher, M. Hilzenthaler, M. Galetz, U. Glatzel, Oxygen diffusion hardened zirconium alloy ZrNb7 – Tribological properties derived from Calo wear and wheel on flat experiments, Tribology International 165 (2022) 107304. https://doi.org/10.1016/j.triboint.2021.107304.

[12] M.C. Galetz, S.H. Seiferth, B. Theile, U. Glatzel, Potential for adhesive wear in friction couples of UHMWPE running against oxidized zirconium, titanium nitride coatings, and cobalt-chromium alloys, Journal of Biomedical Materials Research Part B: Applied Biomaterials 93B (2010) 468–475. https://doi.org/10.1002/jbm.b.31604.

[13] M.C. Galetz, E.W. Fleischmann, C.H. Konrad, A. Schuetz, U. Glatzel, Abrasion resistance of oxidized zirconium in comparison with CoCrMo and titanium nitride coatings for artificial knee joints, Journal of Biomedical Materials Research Part B: Applied Biomaterials 93B (2010) 244–251. https://doi.org/10.1002/jbm.b.31581.

[14] B. Chen, L. Zhuo, Latest progress on refractory high entropy alloys: Composition, fabrication, post processing, performance, simulation and prospect, International Journal of Refractory Metals and Hard Materials 110 (2023) 105993. https://doi.org/10.1016/j.ijrmhm.2022.105993.

[15] B. Gorr, S. Schellert, F. Müller, H.-J. Christ, A. Kauffmann, M. Heilmaier, Current status of research on the oxidation behavior of refractory high entropy alloys, Adv. Eng. Mater. (2021) 2001047. https://doi.org/10.1002/adem.202001047.

[16] Jian Chen, Xueyang Zhou, Weili Wang, Bingyao Liu, Yukun Lv, Wei Yang, Dapeng Xu, Yong Liu, A review on fundamental of high entropy alloys with promising high–temperature properties, Journal of Alloys and Compounds null (2018) null. https://doi.org/10.1016/J.JALLCOM.2018.05.067.

[17] M. Srikanth, A. Annamalai, A. Muthuchamy, C. Jen, A Review of the Latest Developments in the Field of Refractory High-Entropy Alloys, Crystals 11 (2021) 612. https://doi.org/10.3390/CRYST11060612.

[18] Poresh Kumar, T. Lam, P. Tripathi, S. Singh, P. Liaw, E. Huang, Recent progress in oxidation behavior of high-entropy alloys: A review, APL Materials null (2022) null. https://doi.org/10.1063/5.0116605.

[19] K. Lo, H. Murakami, U. Glatzel, J. Yeh, S. Gorsse, An-Chou Yeh, Elemental effects on the oxidation of refractory compositionally complex alloys, International Journal of

Refractory Metals and Hard Materials null (2022) null. https://doi.org/10.1016/j.ijrmhm.2022.105918.

[20] S. Sheikh, M.K. Bijaksana, A. Motallebzadeh, S. Shafeie, A. Lozinko, L. Gan, T.-K. Tsao, U. Klement, D. Canadinc, H. Murakami, S. Guo, Accelerated oxidation in ductile refractory high-entropy alloys, Intermetallics 97 (2018) 58–66. https://doi.org/10.1016/j.intermet.2018.04.001.

[21] J. Jayaraj, P. Thirathipviwat, J. Han, A. Gebert, Microstructure, mechanical and thermal oxidation behavior of AlNbTiZr high entropy alloy, Intermetallics 100 (2018) 9–19. https://doi.org/10.1016/j.intermet.2018.05.015.

[22] C.-H. Chang, M.S. Titus, J.-W. Yeh, Oxidation behavior between 700 and 1300 °C of refractory TiZrNbHfTa high-entropy alloys containing aluminum, Adv. Eng. Mater. 20 (2018) 1700948. https://doi.org/10.1002/adem.201700948.

[23] C. Gadelmeier, Y. Yang, U. Glatzel, E.P. George, Creep strength of refractory high-entropy alloy TiZrHfNbTa and comparison with Ni-base superalloy CMSX-4, Cell Reports Physical Science (2022) 100991. https://doi.org/10.1016/j.xcrp.2022.100991.

[24] E.P. George, D. Raabe, R.O. Ritchie, High-entropy alloys, Nat Rev Mater 4 (2019) 515–534. https://doi.org/10.1038/s41578-019-0121-4.

[25] M. Schütze, Stress Effects in High Temperature Oxidation, in: R.A. Cottis (Ed.), Basic concepts, high temperature corrosion, fourthth ed., Elsevier, 2010, pp. 153–179.

[26] H.E. Evans, Stress effects in high temperature oxidation of metals, International Materials Reviews 40 (1995) 1–40. https://doi.org/10.1179/imr.1995.40.1.1.

[27] A.M. Huntz, M. Schütze, Stresses generated during oxidation sequences and high temperature fracture, Materials at High Temperatures 12 (1994) 151–161. https://doi.org/10.1080/09603409.1994.11689481.

[28] N.D. Stepanov, N. Yurchenko, S.V. Zherebtsov, M.A. Tikhonovsky, G.A. Salishchev, Aging behavior of the HfNbTaTiZr high entropy alloy, Materials Letters 211 (2018) 87–90. https://doi.org/10.1016/j.matlet.2017.09.094.

[29] S.Y. Chen, Y. Tong, K.-K. Tseng, J.-W. Yeh, J.D. Poplawsky, J.G. Wen, M.C. Gao, G. Kim, W. Chen, Y. Ren, R. Feng, W.D. Li, P.K. Liaw, Phase transformations of HfNbTaTiZr high-entropy alloy at intermediate temperatures, Scripta Materialia 158 (2019) 50–56. https://doi.org/10.1016/j.scriptamat.2018.08.032.

[30] S.-M. Chen, Z.-J. Ma, S. Qiu, L.-J. Zhang, S.-Z. Zhang, R. Yang, Q.-M. Hu, Phase decomposition and strengthening in HfNbTaTiZr high entropy alloy from first-principles

calculations, Acta Materialia 225 (2022) 117582. https://doi.org/10.1016/j.actamat.2021.117582.

[31] B. Schuh, B. Völker, J. Todt, N. Schell, L. Perrière, J. Li, J.P. Couzinié, A. Hohenwarter, Thermodynamic instability of a nanocrystalline, single-phase TiZrNbHfTa alloy and its impact on the mechanical properties, Acta Materialia 142 (2018) 201–212. https://doi.org/10.1016/j.actamat.2017.09.035.

[32] P. Kofstad, High Temperature Corrosion, Elsevier, London, 1988.

[33] A. Motallebzadeh, N.S. Peighambardoust, S. Sheikh, H. Murakami, S. Guo, D. Canadinc, Microstructural, mechanical and electrochemical characterization of TiZrTaHfNb and Ti1.5ZrTa0.5Hf0.5Nb0.5 refractory high-entropy alloys for biomedical applications, Intermetallics 113 (2019) 106572. https://doi.org/10.1016/j.intermet.2019.106572.

[34] Č. Jovalekić, M. Zdujić, D. Poleti, L. Karanović, M. Mitrić, Structural and electrical properties of the 2Bi2O3·3ZrO2 system, Journal of Solid State Chemistry 181 (2008) 1321–1329. https://doi.org/10.1016/j.jssc.2008.02.038.

[35] National Bureau of Standards, Standard X-ray diffraction Powder Paterns: Monograph 25 - Section 20, 1984.

[36] National Bureau of Standards, Standard X-ray diffraction powder paterns: Monograph 25 - Section 7, 1969.

[37] B. Song, Y. Yang, M. Rabbani, T.T. Yang, K. He, X. Hu, Y. Yuan, P. Ghildiyal, V.P. Dravid, M.R. Zachariah, W.A. Saidi, Y. Liu, R. Shahbazian-Yassar, In situ oxidation studies of high-entropy alloy nanoparticles, ACS Nano 14 (2020) 15131–15143. https://doi.org/10.1021/acsnano.0c05250.

[38] M. Garg, H.S. Grewal, R.K. Sharma, B. Gwalani, H.S. Arora, High oxidation resistance of AlCoCrFeNi high entropy alloy through severe shear deformation processing, Journal of Alloys and Compounds 917 (2022) 165385. https://doi.org/10.1016/j.jallcom.2022.165385.

[39] H. Okamoto, O-Ti (Oxygen-Titanium), J. Phase Equilib. Diffus. 32 (2011) 473–474. https://doi.org/10.1007/s11669-011-9935-5.

[40] J.P. Abriata, J. Garcés, R. Versaci, The O−Zr (Oxygen-Zirconium) system, Bulletin of Alloy Phase Diagrams 7 (1986) 116–124. https://doi.org/10.1007/BF02881546.

[41] E. Rudy, P. Stecher, Zum Aufbau des Systems Hafnium-Sauerstoff, Journal of the Less Common Metals 5 (1963) 78–89. https://doi.org/10.1016/0022-5088(63)90045-6.

[42] J. Luo, W. Sun, R. Duan, W. Yang, K.C. Chan, F. Ren, X.-S. Yang, Laser surface treatment-introduced gradient nanostructured TiZrHfTaNb refractory high-entropy alloy

with significantly enhanced wear resistance, Journal of Materials Science & Technology 110 (2022) 43–56. https://doi.org/10.1016/j.jmst.2021.09.029.

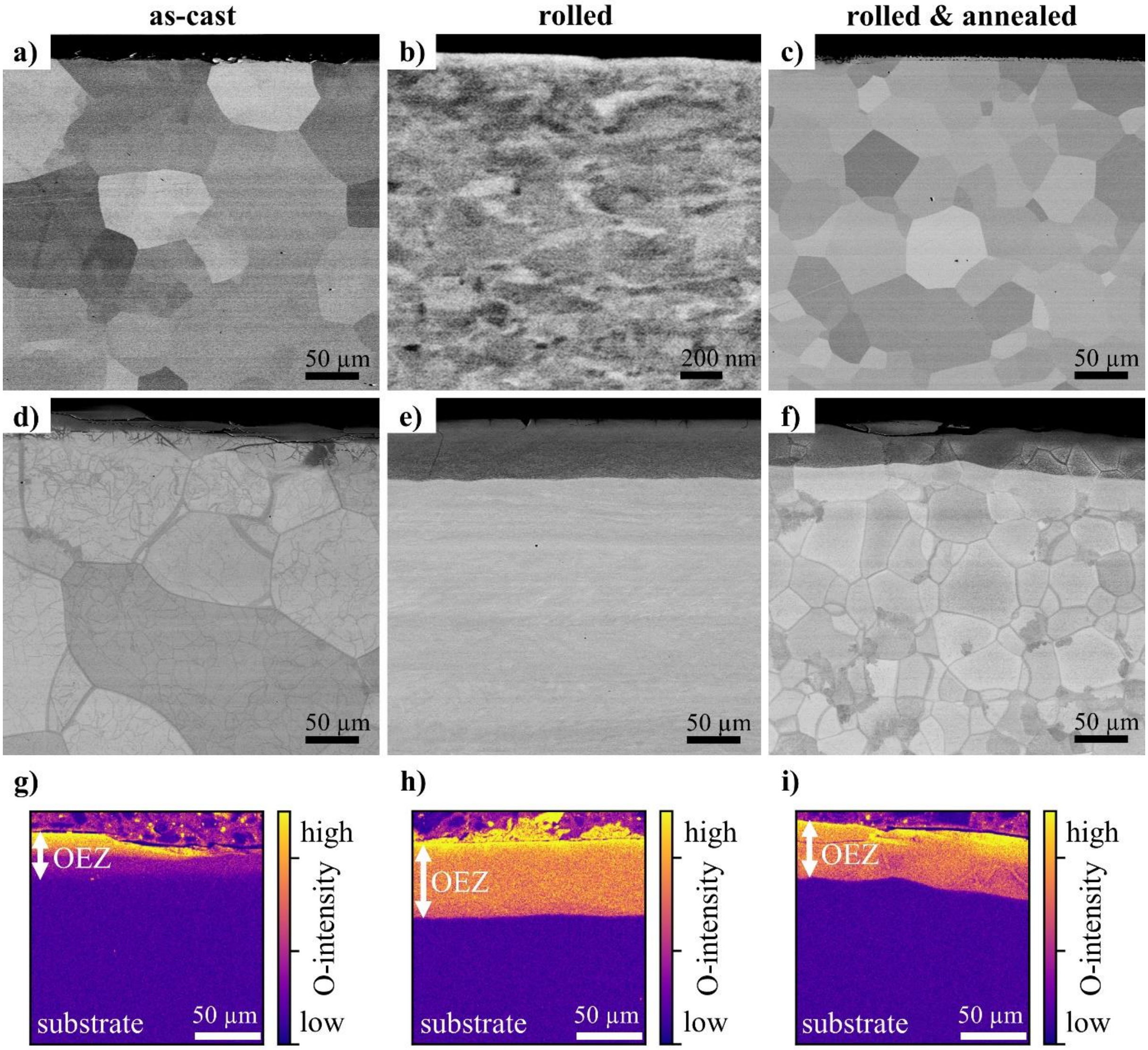

Figure 1: Micrographs showing the microstructure of the as-cast, rolled, and rolled & annealed state before (a-c) and after 24 h of oxidation in synthetic air at 600 °C (d-e), including EPMA oxygen mappings indicating a surface-near oxygen-enriched zone (OEZ) and a non-oxygen-enriched substrate (g-i).

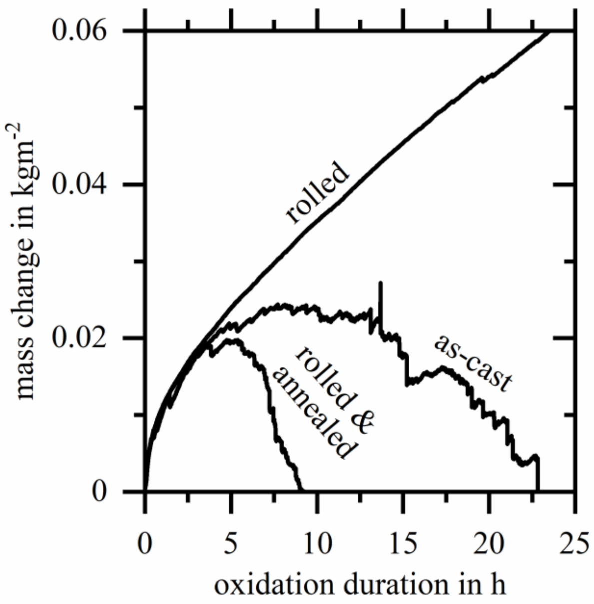

Figure 2: Mass change per surface area during oxidation at 600°C in synthetic air of an as-cast, a rolled, and a rolled & annealed specimen.

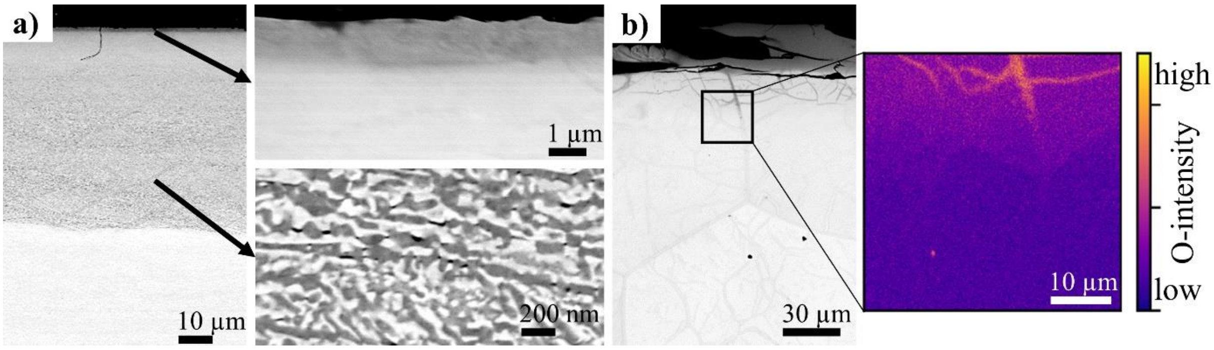

Figure 3: Micrographs showing the oxygen-enriched zone of the rolled (a) and as-cast TiZrNbHfTa in combination with an EPMA oxygen mapping (b) after oxidation for 24 h at 600 °C.

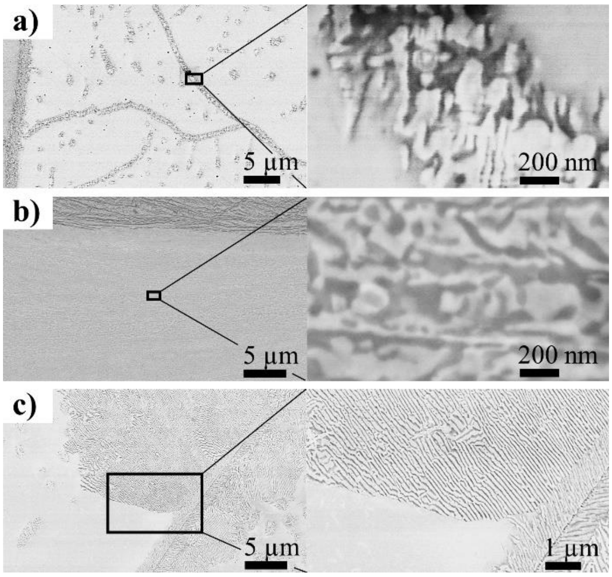

Figure 4: Micrographs showing the phase transformation in the non-oxygen-enriched substrate of as-cast (a), rolled (b), and rolled & annealed (c) TiZrNbHfTa after 24 h of oxidation at 600 °C.

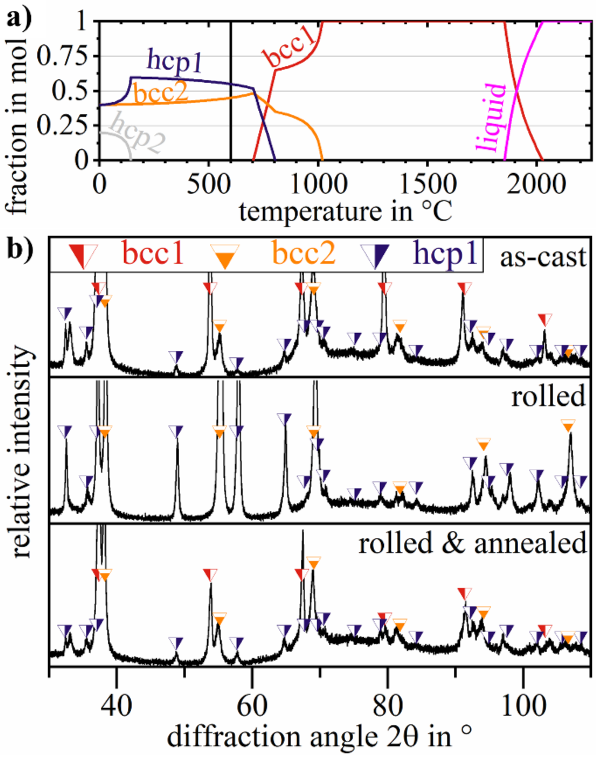

Figure 5: Predicted Thermocalc TiZrNbHfTa phase diagram (a) and identified phases in experimental XRD diffractograms of the non-oxygen-enriched substrates of as-cast, rolled, and rolled & annealed TiZrNbHfTa after 24 h of oxidation at 600 °C (b).

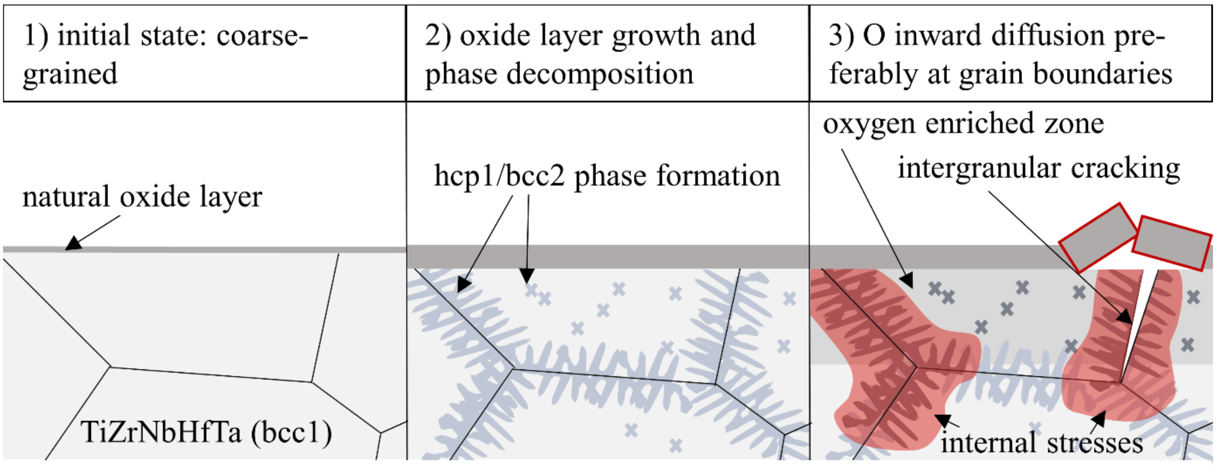

mechanism:

- localized phase decomposition preferably at (sub)grain boundaries
- localized, rapid oxygen diffusion along grain boundaries
- localized oxygen dissolution or internal oxidation along grain boundaries
- ➢ localized internal stresses and intergranular cracking
- ➢ spallation

Figure 6: Schematic oxidation process of coarse-grained as-cast and rolled & annealed TiZrNbHfTa at 600 °C in air.

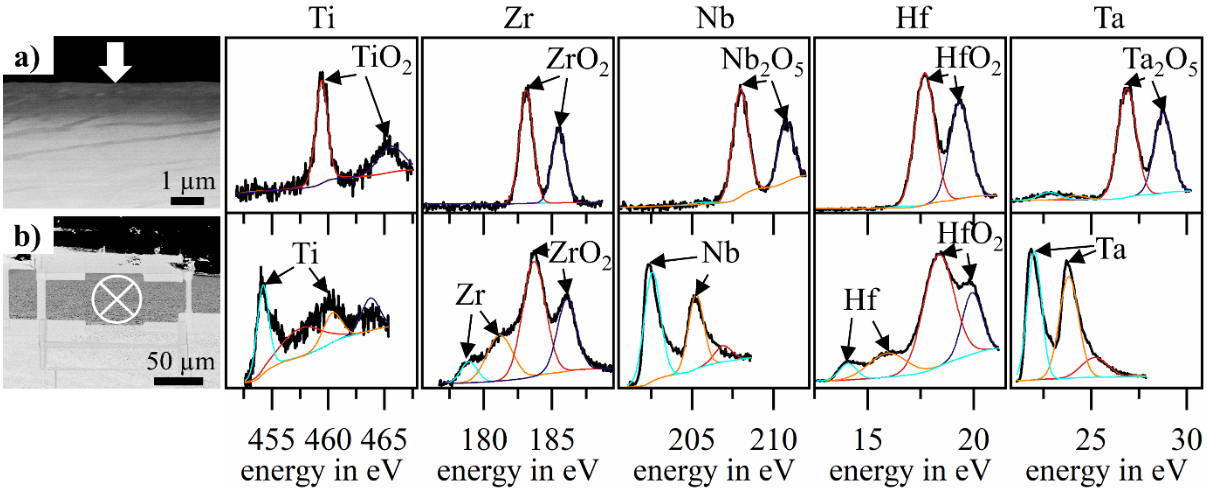

Figure 7: XPS surface analysis on rolled TiZrNbHfTa after 1 h of oxidation at 600 °C (a) and XPS cross-sectional analysis within a masked target region on rolled TiZrNbHfTa after 24 h of oxidation at 600 °C (b).

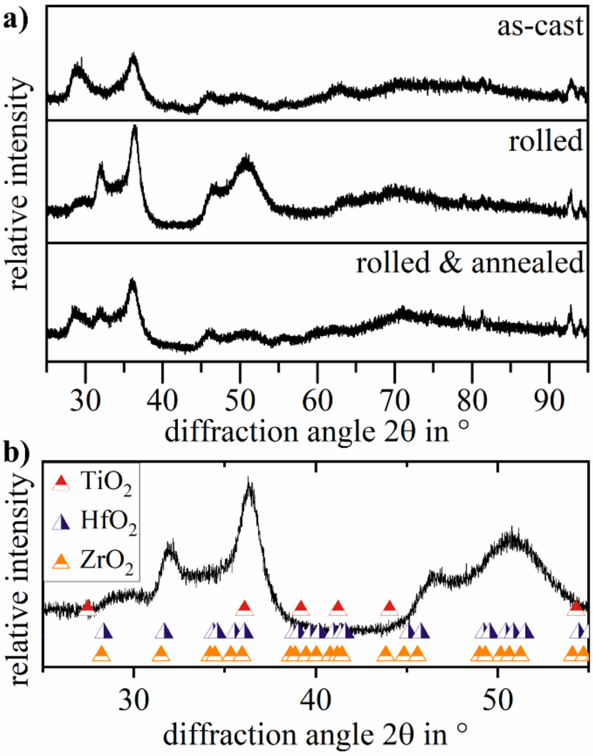

Figure 8: XRD measurements on the oxidized surface of as-cast, rolled, and rolled & annealed TiZrNbHfTa after 24 h of oxidation at 600 °C (a) with a magnified excerpt for the rolled material including added indicators of the theoretical reflex positions of TiO_2 (ICDD 00-021-1276), HfO_2 (ICDD 00-034-0104), and ZrO_2 (ICDD 04-015-6852)(b).

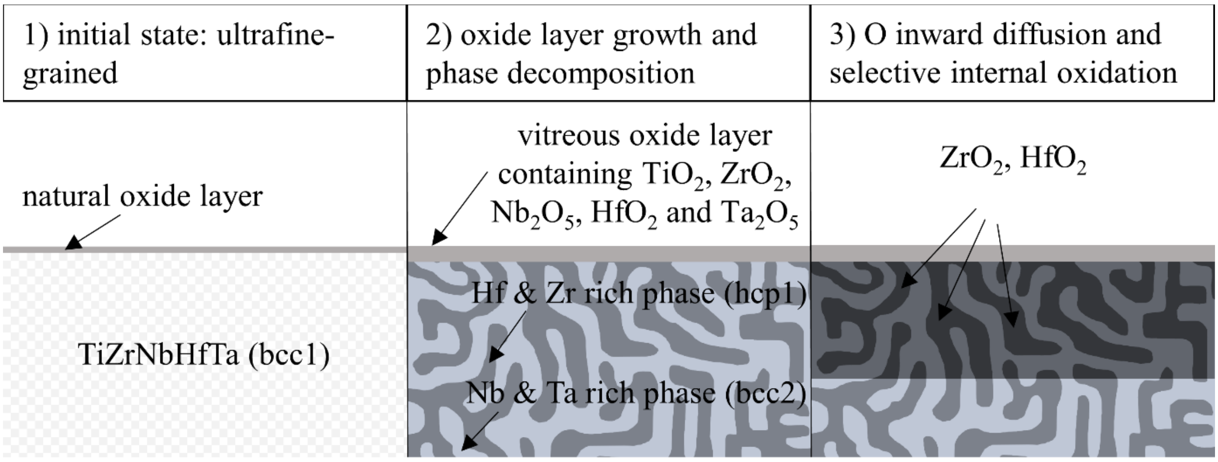

mechanism:

- homogeneous phase decomposition throughout the specimen
- homogeneous oxygen inward diffusion throughout the specimen
- internal oxidation of Hf and Zr

➢ no localized internal stresses and intergranular cracking
➢ adherent surface oxide layer

Figure 9: Schematic oxidation process of ultrafine-grained rolled TiZrNbHfTa at 600 °C in air.

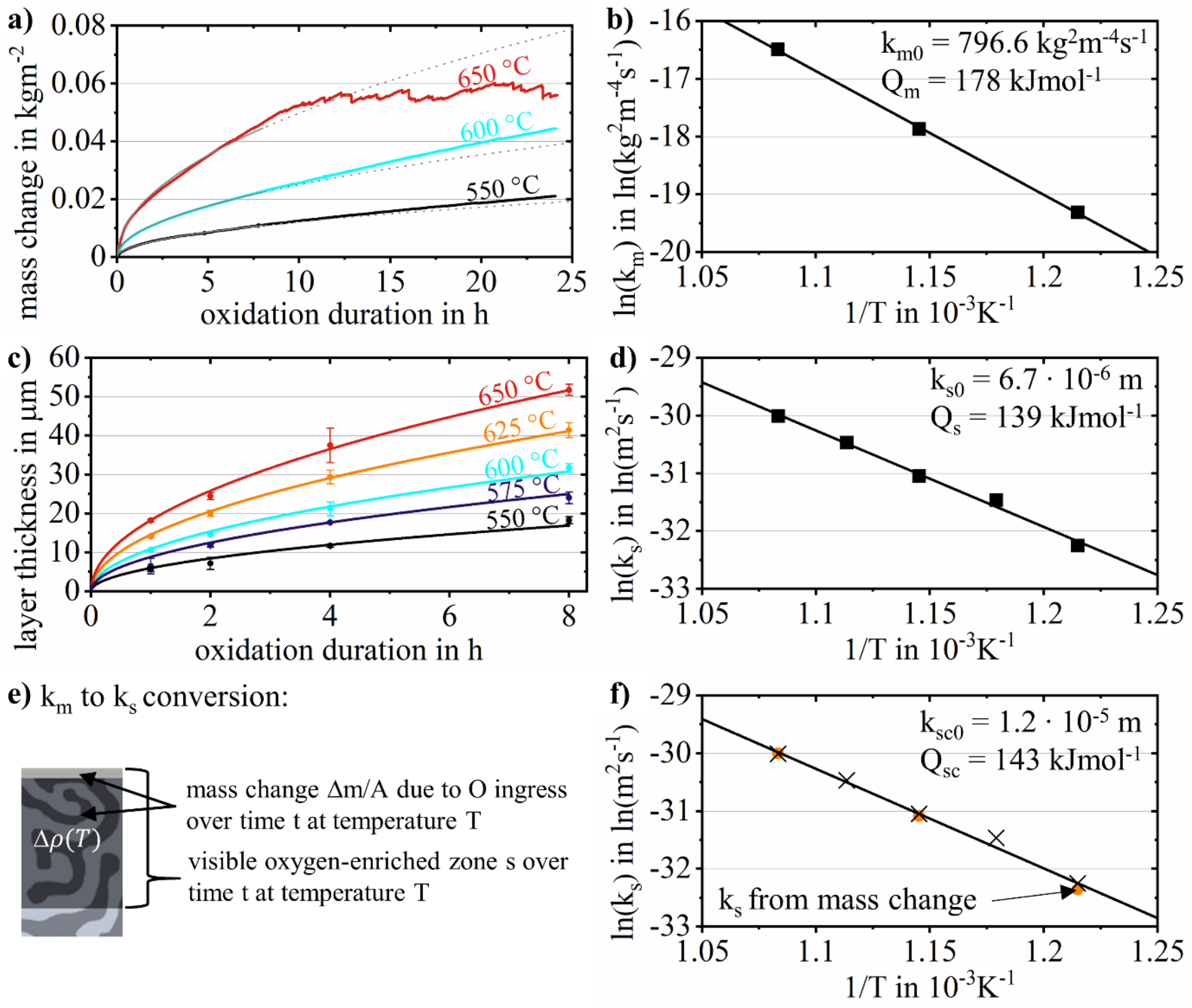

Figure 10: Mass change of as-rolled TiZrNbHfTa during oxidation in synthetic air at 550 °C, 600 °C, and 650 °C (a) with corresponding Arrhenius plot (b), and growth of the oxygen-enriched zone during oxidation in air in the temperature range 550 °C – 650 °C (c) with corresponding Arrhenius plot (d). A conversion of the mass change-related reaction constants k_m into the reaction constants k_s based on the thickness of the oxygen-enriched zone according to (e) yields a combined Arrhenius plot (f).

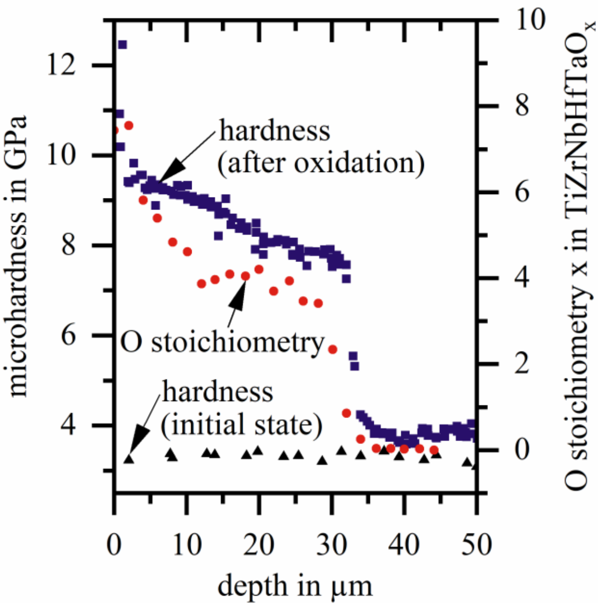

Figure 11: Microhardness-depth profile of rolled TiZrNbHfTa after oxidation at 600 °C for 8 h and the corresponding oxygen concentration-depth profile expressed in terms of oxygen stoichiometry as derived from nuclear reaction analysis. The microhardness-depth profile of rolled TiZrNbHfTa in the initial state is provided for comparison.

Table 1: Bulk elemental concentrations determined via µX-ray fluorescence analysis (Ti, Zr, Nb, Hf, Ta) and carrier hot gas extraction analysis (O, N)

Element concentrations in at. %	Ti	Zr	Nb	Hf	Ta	O	N
as-cast	18.4	21.7	20.8	20.1	18.6	0.25	0.11
rolled	18.0	21.2	21.1	19.9	19.4	0.31	0.15
rolled & annealed	18.0	20.4	21.0	20.2	19.9	0.34	0.13